Cell, Volume *139*

Cytoskeletal Forces Span the Nuclear Envelope to Coordinate Meiotic Chromosome Pairing and Synapsis

Aya Sato, Berith Isaac, Carolyn M. Phillips, Regina Rillo, Peter M. Carlton, David J. Wynne, Roshni A. Kasad, and Abby F. Dernburg

Supplemental Results

HTP-1 and SUN-1 act independently to inhibit non-homologous synapsis

The non-homologous synapsis we observed after partial depletion of SUN-1 by RNAi, together with the shorter transition zone phenotype of *sun-1(jf18)* animals (Penkner et al., 2007), suggest that SUN-1 might act both to prevent promiscuous synapsis and to sustain the phase of meiosis during which pairing is actively promoted. This is similar to a proposed role for the axial element component HTP-1*,* mutations in which also lead to extensive non-homologous synapsis and an abbreviated transition zone, even when synapsis is prevented (Couteau and Zetka, 2005; Martinez-Perez and Villeneuve, 2005). We directly compared the phenotypes of *htp-1(gk174)* and *sun-1(jf18)* mutations with respect to chromosome pairing, NE patch formation, and synapsis. First, as previously reported, *htp-1(gk174)* animals display almost normal levels of *X* chromosome pairing despite severely impaired autosome pairing (Couteau and Zetka, 2005; Martinez-Perez and Villeneuve, 2005), while *sun-1(jf18)* animals show severely impaired pairing of all chromosomes (Penkner et al., 2007). Second, a short region of the gonad containing nuclei with small and dispersed NE patches and polarized nuclear morphology was detected in the *htp-1(gk174)* gonads (Figure S14)*.* Markedly fewer nuclei displayed polarized nuclear morphology in *sun-1(jf18)* gonads, and distinct NE patches were not observed by SUN-1 or ZYG-12 immunofluorescence (Figure S6). (We note, however, that small foci of SUN-1^{jf18} were detected by imaging of the GFP-tagged mutant protein in the accompanying work by Penkner *et al*.) The more prominent hallmarks of the transition zone in *htp-1(gk174)* mutants may partially explain the ability of *X* chromosomes to achieve pairing in *htp-1* but not in *sun-1* mutants/RNAi. Third, in *htp-1(gk174)* animals, SC polymerization was not observed along all axial elements until late pachytene; chromosomes initiated non-homologous synapsis prematurely in the transition zone*,* but extensive regions lacked SYP-1 staining in early and mid-pachytene. Non-homologous synapsis in *sun-1(jf18)* animals was far more robust, such that axial regions lacking SYP-1 were largely absent by early pachytene (Figure 6)*.* This suggests that HTP-1 may promote the processivity of SC polymerization, in addition to inhibiting non-homologous synapsis.

To probe the functional relationship between SUN-1 and HTP-1, we generated a strain carrying mutations in both genes. Homozygous *htp-1(gk174); sun-1(jf18)* animals showed severely impaired *X* chromosome pairing and extensive non-homologous synapsis, like *sun-1(jf18)* mutants (Figure S14). However, the progression of SC

polymerization resembled that seen in *htp-1(gk174)*, in that unsynapsed regions were evident until late pachytene. In other words, double mutants displayed a hybrid phenotype that combined the *X*-chromosome pairing defect of *sun-1(jf18)* with the less extensive SC polymerization of *htp-1(gk174)*. Like *sun-1(jf18)* mutants, the double mutant gonads had very few nuclei with polarized chromosomes and no obvious NE patches (Figure S14). Taken together, it seems that *sun-1* and *htp-1* play independent roles, although both are required to impose the normal barrier(s) to non-homologous synapsis.

We tested whether the requirement for dynein to initiate synapsis is dependent on *htp-1* by depleting dynein in *htp-1(gk174)* animals. Extensive non-homologous synapsis was observed in *dhc-1(or195); htp-1(gk174); dlc-1(RNAi)* animals at restrictive temperature (50 hrs of RNAi, 24 hrs at 25˚C) (Figure S14). Thus, loss of either *sun-1* or *htp-1* is sufficient to release SC polymerization from its dependence on dynein, but the resulting polymerization occurs aberrantly, between non-homologous chromosomes.

SUN-1 and ZYG-12 are dispensable for PC association with the NE.

To further investigate the interdependence of SUN-1, ZYG-12 and dynein in their NE localization, we isolated a *zyg-12* deletion (see Supplemental Experimental Procedures). The *zyg-12(ie14)* allele removes 331 bp, truncating any potential protein before the transmembrane and KASH domains. Homozygous *zyg-12(ie14)* adults from heterozygous parents showed severe germline developmental defects, and were sterile, similar to *sun-1(gk199)* animals. No dynein was detected at the NE in *zyg-12(ie14)* gonads by immunofluorescence (data not shown). SUN-1 was distributed evenly at the NE and did not form patches in *zyg-12(ie14)* gonads, indicating that interaction between SUN-1 and ZYG-12 is required to mediate concentration of SUN-1 within the inner NE (Figure S11A). We conclude that dynein requires ZYG-12, which in turn requires SUN-1, to localize at the NE in meiotic nuclei, consistent with previous observations in mitotic cells (Malone et al., 2003), and that SUN-1 and ZYG-12 are both required for the meiosis-specific appearance of NE patches.

Reduction by half of the gene dosage of either *sun-1* or *zyg-12* did not result in any detectable defects on their own, but did enhance the severity of segregation defects when combined with a heterozygous deficiency of the *X* chromosome PC (Table S1), consistent with our other data that these proteins contribute to the role of PCs in meiotic chromosome segregation. Animals carrying deletion alleles of *sun-1(gk199)* or *zyg-12(ie14)* showed extensive loading of both the axial elements and transverse filaments of the SC as linear stretches on chromosomes. Axial element morphogenesis occurred on schedule, based on staining with HTP-3 antibodies. Extensive SYP-1 loading along chromosomes was observed in both deletion alleles (Figure S11B), indicating that the polymerization of SC does not require SUN-1 or ZYG-12. Due to severe polyploidy, we were unable to determine if the extensive synapsis was between homologous or non-homologous regions, but together with our other analysis, it seems likely that SC formation in these mutants occurs in the absence of normal homolog pairing. These observations indicate that both SUN-1 and ZYG-12 play inhibitory roles in SC formation.

Supplemental Experimental Procedures

Isolation of the *zyg-12 (ie14)* deletion mutant

zyg-12(ie14) was isolated by screening a library of worms mutagenized with TMP/UV using the "poison primer" approach (Edgley et al., 2002). Sequencing identified a 331-bp deletion that removes nucleotides 1583 to 1913 in the *zyg-12* ORF, resulting in a frame shift and early stop codon. This truncated version of ZYG-12 includes the intact N-terminal half of the amino acid sequence (1-479 aa) but is predicted to lack the transmembrane and KASH domains.

High Resolution Real-time Imaging of ZYG-12:GFP patch motion

Young hermaphrodites were placed into a 10-µl drop of M9 buffer containing 0.1% tricaine and 0.01% tetramisole (Sigma) on top of a pad of 2% agarose in M9 buffer on a microscope slide. When worms stopped moving, a coverslip was placed on top, and the slide was inverted and placed on the microscope. Live imaging was carried out using wide-field optical sectioning microcopy, and 3D data stacks were deconvolved with a measured point-spread function (PSF). Excitation light was provided by a solid-state 488nm laser attenuated to 10% transmission with a neutral density filter. A piezoelectric stage provided rapid translation in Z, and an EMCCD camera (Andor Ixon) was used to record images at a frame rate of 30 Hz. Worms were routinely removed from pads and produced viable progeny post-imaging (data not shown).

Transmission Electron Microscopy and EM Tomography

Whole worms were fixed by high-pressure freezing (HPF; Muller-Reichert et al., 2003) followed by freeze-substitution. To facilitate longitudinal sectioning of the animals, hermaphrodites were transferred to a slot grid covered with *E. coli* paste, placed on a type B HPF planchette, which was covered with another type B planchette immediately before freezing.

Freeze substitution was carried out in anhydrous acetone containing 0.2% Ethylene Glycol bis (Succinimidyl succinate) (EGS, Pierce), using an automated freeze substitution machine (Leica Microsystems, Wetzlar, Germany). Samples were maintained at -90°C for 3 days, then allowed to warm to -25°C at a rate of 5°C per hour, and to room temperature at a rate of 10°C per hour. Samples were then gradually infiltrated with Epon resin. Single worms were distributed evenly in Epon on a glass slide, and samples were polymerized at 60°C for 24 hours. Individual worms were then mounted on dummy blocks. For thin-section TEM, serial thin sections (~70 nm) were cut using a Leica Ultracut E microtome. Sections were collected on Formvar-coated copper slot grids. The samples were post-stained with 2% uranyl acetate in 50% Ethanol followed by Reynolds' lead citrate and imaged using an FEI Tecnai T12 TEM operated at 120KV. Transition zone nuclei were identified primarily by the asymmetric position of their nucleoli, and their location near the distal end of the gonad.

For electron tomography, semi-thick sections (~100 nm) were cut and decorated on both sides with 12-nm colloidal gold to facilitate subsequent image alignment. Double-tilt image series were acquired with an FEI Tecnai F20 TEM operating at 200 kV. Images were recorded on a 4k x 4k TemCam F415 CCD camera (TVIPS). Image

acquisition was performed at 1.5° intervals over a range of 63°, using the SerialEM program for automated tilt series collection (Mastronarde, 2005). Alignment and 3D reconstruction were performed using the IMOD image-processing package (Kremer et al., 1996).

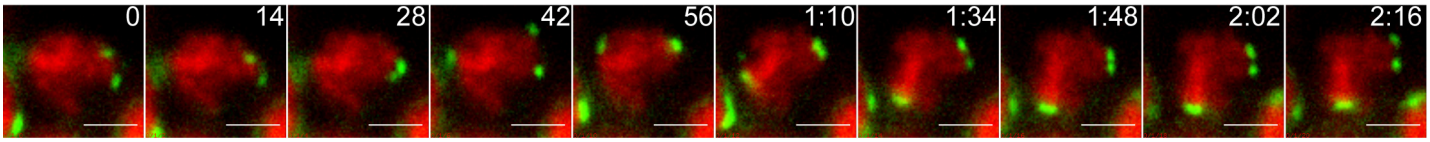

Figure S1. NE patches merge and separate. These images correspond to alternate successive frames from Supplemental Movie 3, acquired at 7-second intervals. Elapsed time since the first frame in seconds is indicated. Single optical sections reveal multiple dynamic patches at the nuclear periphery that appear to fuse and separate over the 2-minute course of this movie. Images were acquired using a DeltaVision RT wide-field deconvolution microscope. Scale bars, 2μm.

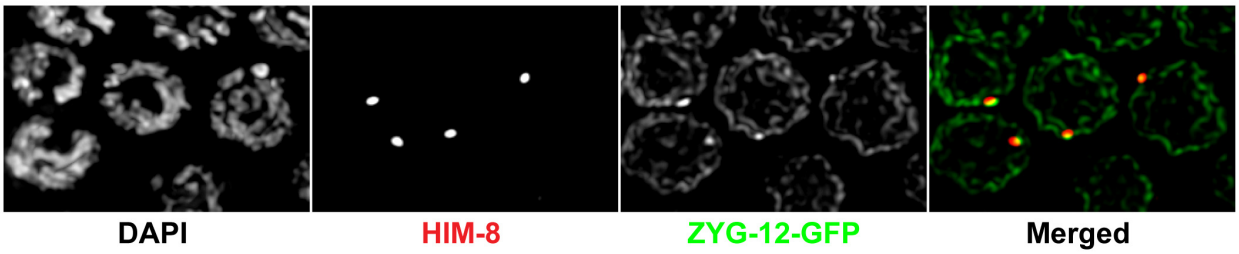

Figure S2. HIM-8 remains associated with a small focus of ZYG-12 throughout the pachytene stage. Maximum-intensity projections showing mid-pachytene nuclei stained with anti-HIM-8 (red), anti-GFP (green) and DAPI, imaged by wide-field deconvolution microscopy.

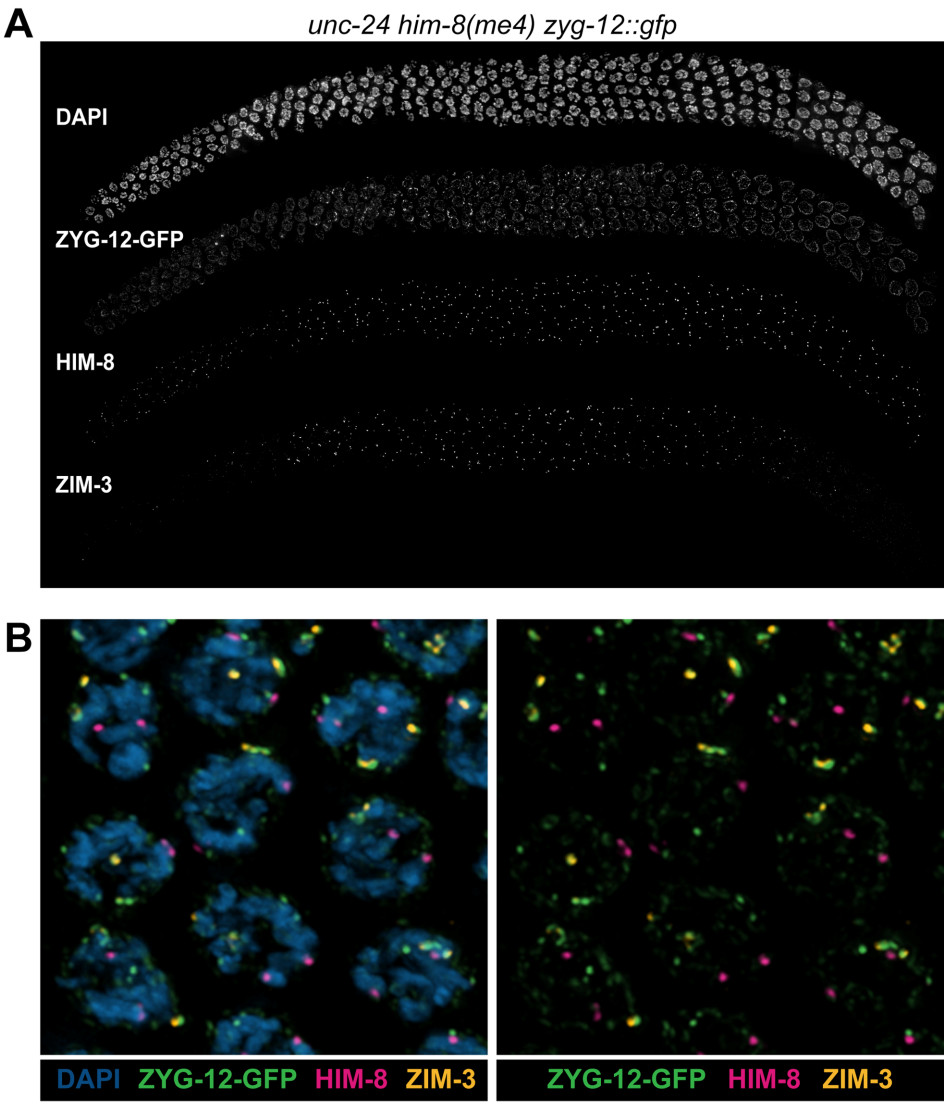

Figure S3. Inhibition of *X* chromosome synapsis results in an extended region of NE patches and associated ZIM foci. Germline nuclei from a *unc-24 him-8(me4) zyg-12::gfp* hermaphrodite, which fails to pair and synapse its *X* chromosomes, are shown at low and high magnification (A and B, respectively). The sample was stained with anti-GFP, anti-HIM-8, and anti-ZIM-3 antibodies, and DAPI. ZIM-3 foci (also ZIM-1 and ZIM-2, not shown here) are clearly detected throughout most of meiotic prophase, by contrast to wild-type animals, where these foci are restricted to the narrow transition zone region (see (Phillips and Dernburg, 2006) for examples). ZIM foci correlate with an extended region of polarized chromosomes and NE patches. B) Merged high-magnification images shown with (left) and without (right) the DAPI image. ZIM-3 is associated with ZYG-12 patches, but HIM-8^{me4} is not (see also Figure 1C). Similar persistence of transition zone features, including NE patches, is seen in other mutants that abrogate synapsis of one or more chromosomes.

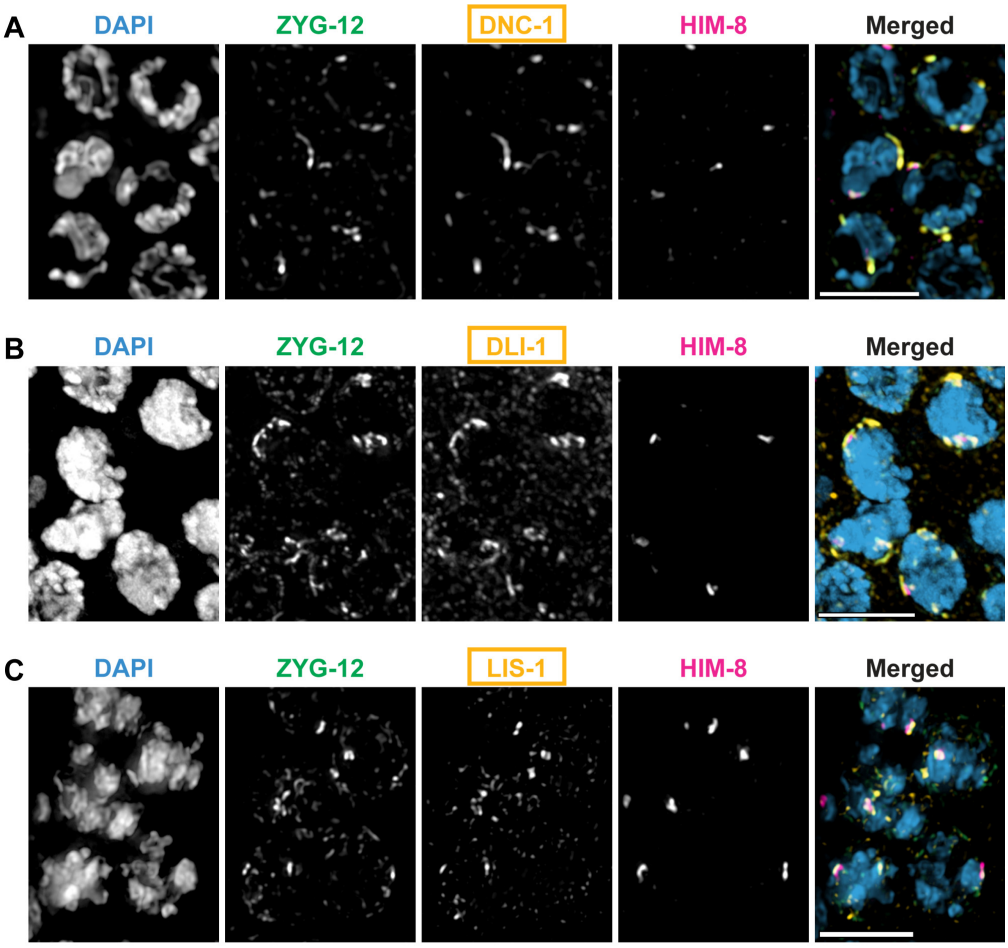

Figure S4. Dynein regulatory components are associated with meiotic NE patches. Wild type hermaphrodites expressing *zyg-12::gfp* were stained with the indicated antibodies: DNC-1 (dynactin), DLI-1 (dynein light intermediate chain) and LIS-1 each concentrate at the ZYG-12 patches. Separate and merged images of 4-μm projections through transition zone nuclei are shown. In the merged images, ZYG-12 is shown in green, DNC-1/DLI-1/LIS-1 in orange, and HIM-8 in magenta. Scale bars, 5 μm.

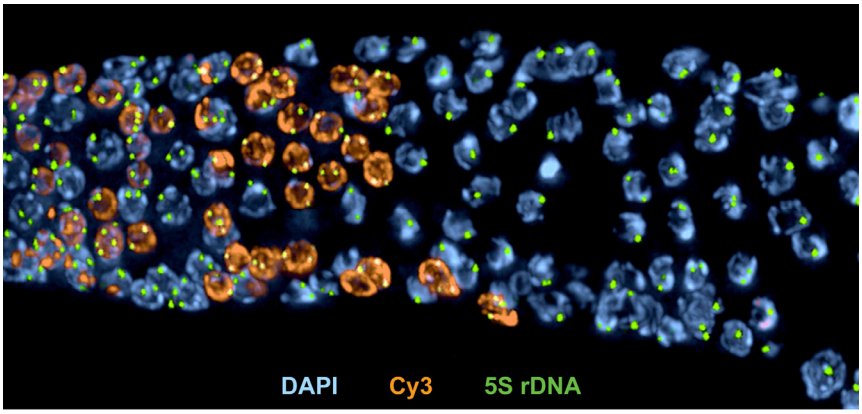

Figure S5. Nuclear polarization and homolog pairing follow meiotic S-phase. A wild-type hermaphrodite was injected with 10 mM Cy3-dUTP to label newly synthesized DNA, allowed to recover for 30 minutes, then dissected and fixed for FISH. A probe to the 5S rDNA locus on Chromosome *V* (green) was hybridized to analyze pairing, and DNA was counterstained with DAPI (blue). Cy3-positive nuclei (orange) all have unpaired FISH signals, indicating that pairing at this locus occurs only after completion of S-phase. Nuclei immediately proximal (to the right, in this image) to the Cy3-labeled zone show polarized morphology and mostly paired FISH signals, indicating that these transition zone features are established shortly after completion of replication.

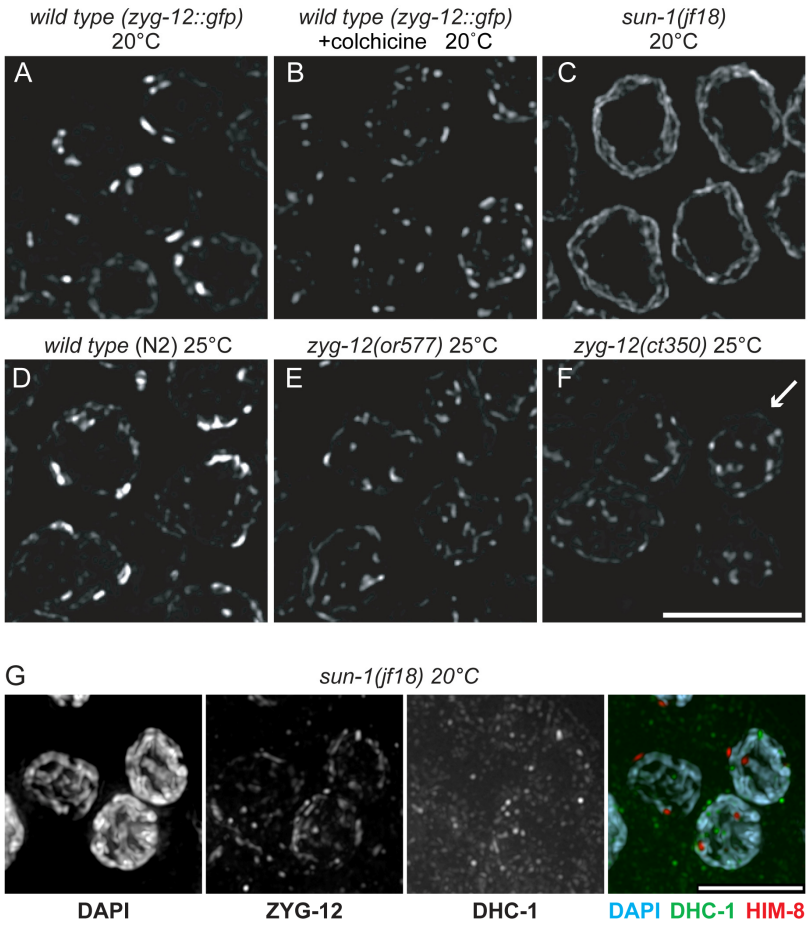

Figure S6. Morphology of meiotic NE patches is altered by disruption of microtubules or by mutation of patch-associated proteins. Maximum-intensity projections of 3D stacks of transition zone nuclei acquired by wide-field deconvolution imaging. NE patches were visualized by immunofluorescence detection of ZYG-12-GFP (A, B) or SUN-1 (C, D, E, F). (A) Wild type *(zyg-12:gfp)* animals at 20˚C. (B) Smaller and more scattered NE patches observed 6 hrs after colchicine injection. (C) NE patches are greatly reduced by the *sun-1(jf18)* mutation. (D, E, F) Wild type (N2), *zyg-12(or577^{ts})* and *zyg-12(ct350^{ts})* animals picked as L4 larvae were kept at 15˚C for 24 hours, shifted to 25˚C for 6 hours and immediately dissected for immunofluorescence. Smaller and more scattered NE patches were observed in *zyg-12*^{ts} mutants. The same staining pattern was observed using ZYG-12 antibodies (data not shown). In F, the arrow indicates a nucleus with twelve small NE patches. Scale bar, 5μm. (G) ZYG-12 localization detected by anti-ZYG-12 was greatly reduced, and DHC-1 was not detectable at the NE in *sun-1(jf18)* animals.

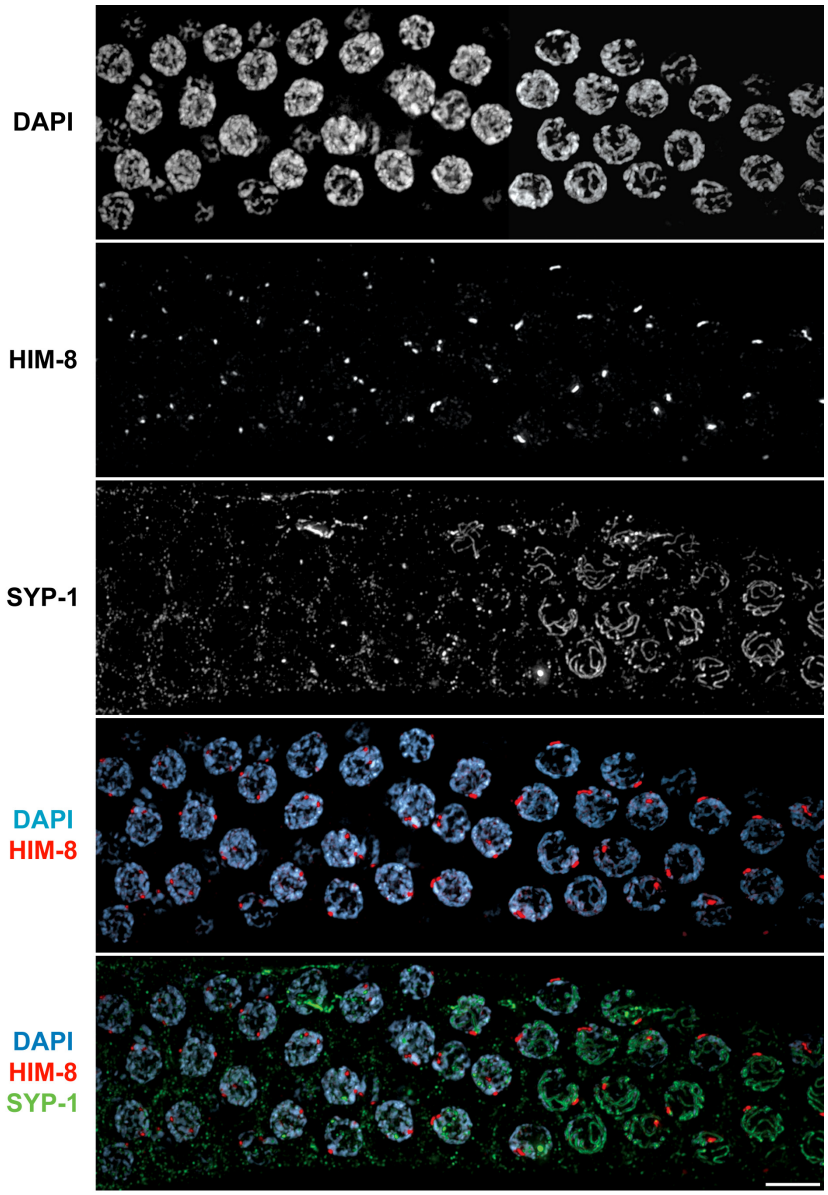

Figure S7. The microtubule destabilizing drug HTI-286 disrupts homolog pairing and polarized nuclear morphology. Wild-type animals were incubated in 1μM HTI-286 for 6 hours, then dissected and stained with anti-SYP-1, anti-HIM-8, and DAPI. Affected animals were identified by an elevated number of mitotic figures (≥10) in the premeiotic region of the gonad (not shown). The regions of the gonad corresponding to the transition zone (left) and early pachytene nuclei (right) are shown. Like colchicine, HTI-286 inhibited homolog pairing among nuclei that were exposed prior to transition zone entry. Polarized morphology, normally indicative of transition zone nuclei, was also disrupted. The nuclei with extensive synapsis in the right portion of the images were likely exposed to the drug only after homolog pairing and synapsis were established. Scale bar, 5 μm.

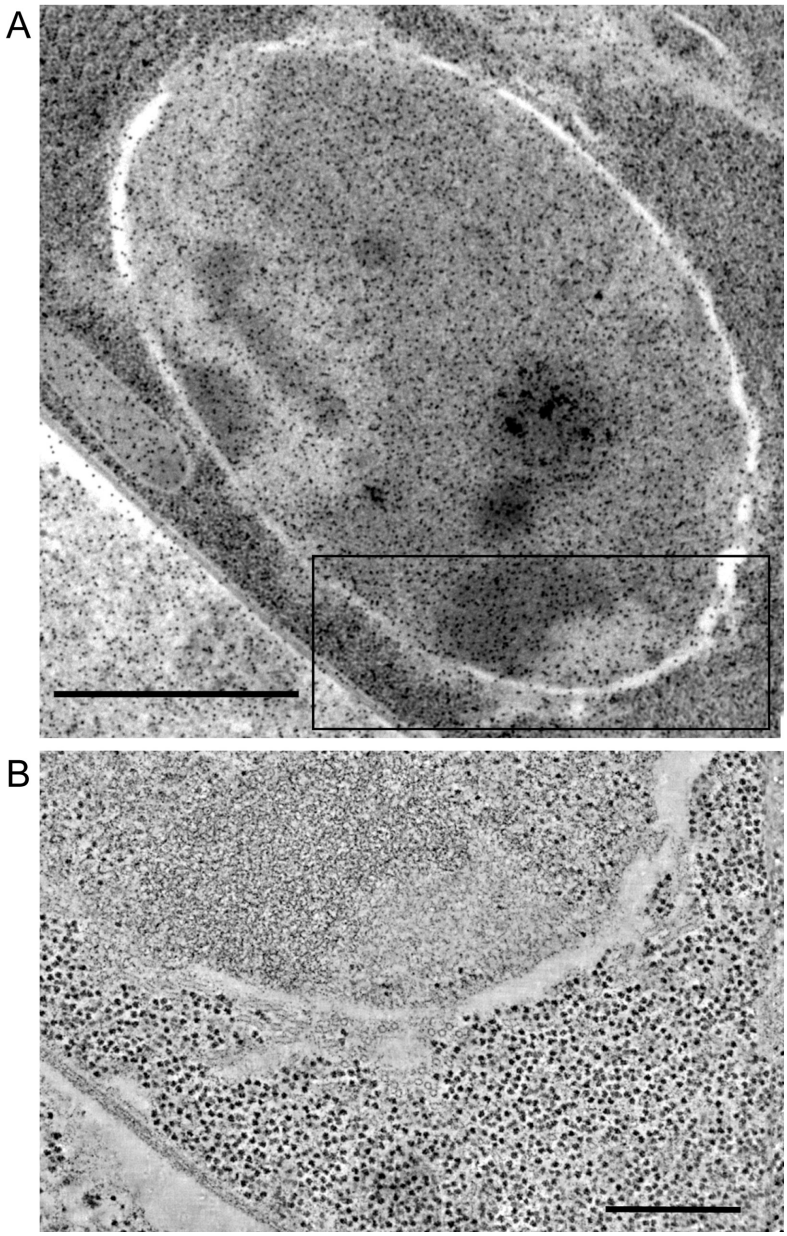

Figure S8. Cytoplasmic microtubules are observed at the outer nuclear surface. A) Low magnification reference view of an EM section through a transition zone nucleus. The electron-dense particles covering the section are colloidal gold used for tomographic alignment. Scale bar, 1µm. B). Tomographic section from a 3D reconstruction, corresponding to the region outlined in (A). Cross-sections and longitudinal sections of individual microtubules are observed along the nuclear periphery, many adjacent to the darker chromatin region. Scale bar, 300 nm.

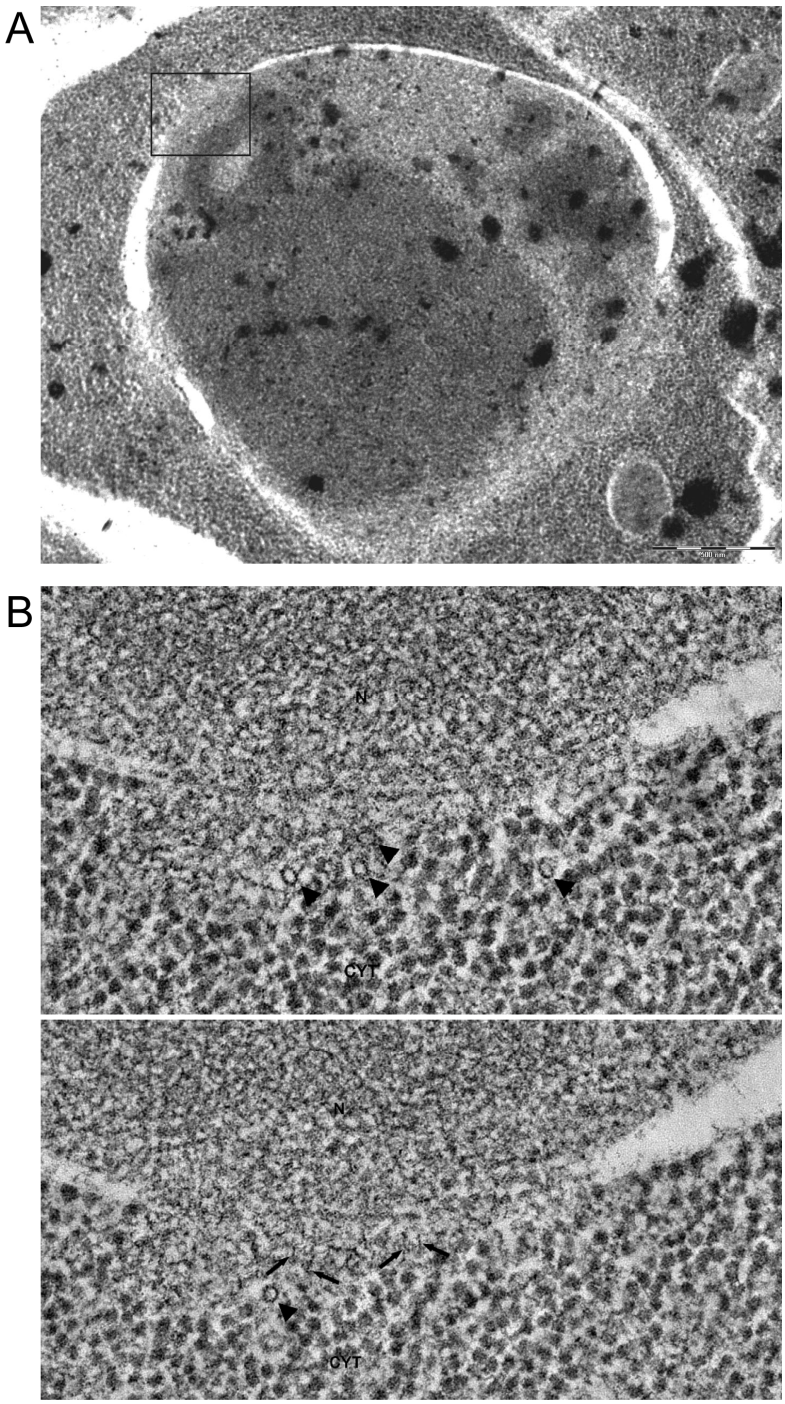

Figure S9. Fibrillar structures are observed at the NE. A) Low magnification reference view of an EM section through transition zone nucleus. Scale bar, 500 nm. B) Two high-magnification sections from a 3D tomogram of the region outlined in A). N=nucleus; CYT=cytoplasm. These sections are about 9 nm apart. Fibrillar structures are particularly evident in the lower image (arrows) where they appear to span the nuclear envelope and protrude into the cytoplasm. Microtubule cross-sections can also be seen in the vicinity (arrowheads).

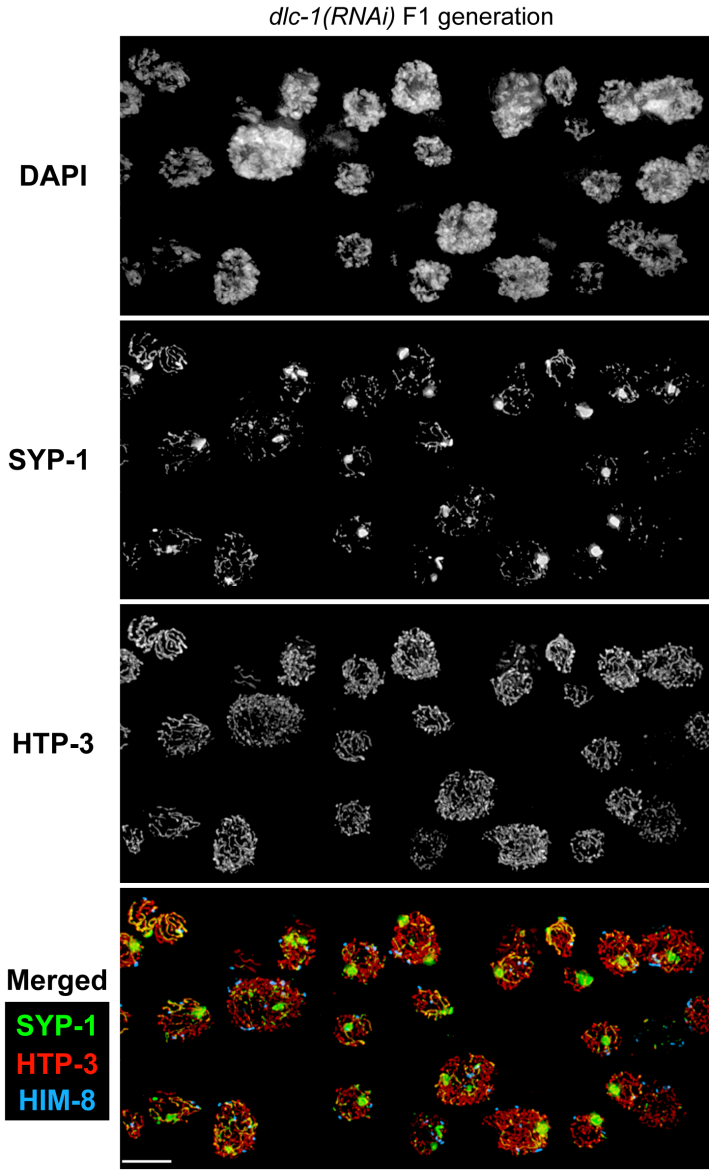

Figure S10. **Depletion of DLC-1 (dynein light chain) results in mitotic and meiotic defects.** Wild type animals (N2 young adults) were subjected to RNAi against *dlc-1* at 20˚C, and their F1 progeny (18 hours post-L4) were dissected for immunofluorescence. The images show maximum-intensity projections from the mid-pachytene region of the gonad, stained with anti-SYP-1(green), anti-HTP-3 (red), anti-HIM-8 (blue) and DAPI. Large aggregates of SYP-1 with some stretches along the chromosomes were observed. The heterogeneity in nuclear size likely reflects mitotic errors prior to meiotic entry; nuclear positioning, which requires dynein function (Zhou et al., 2009), is also disrupted. Scale bar, 5 μm.

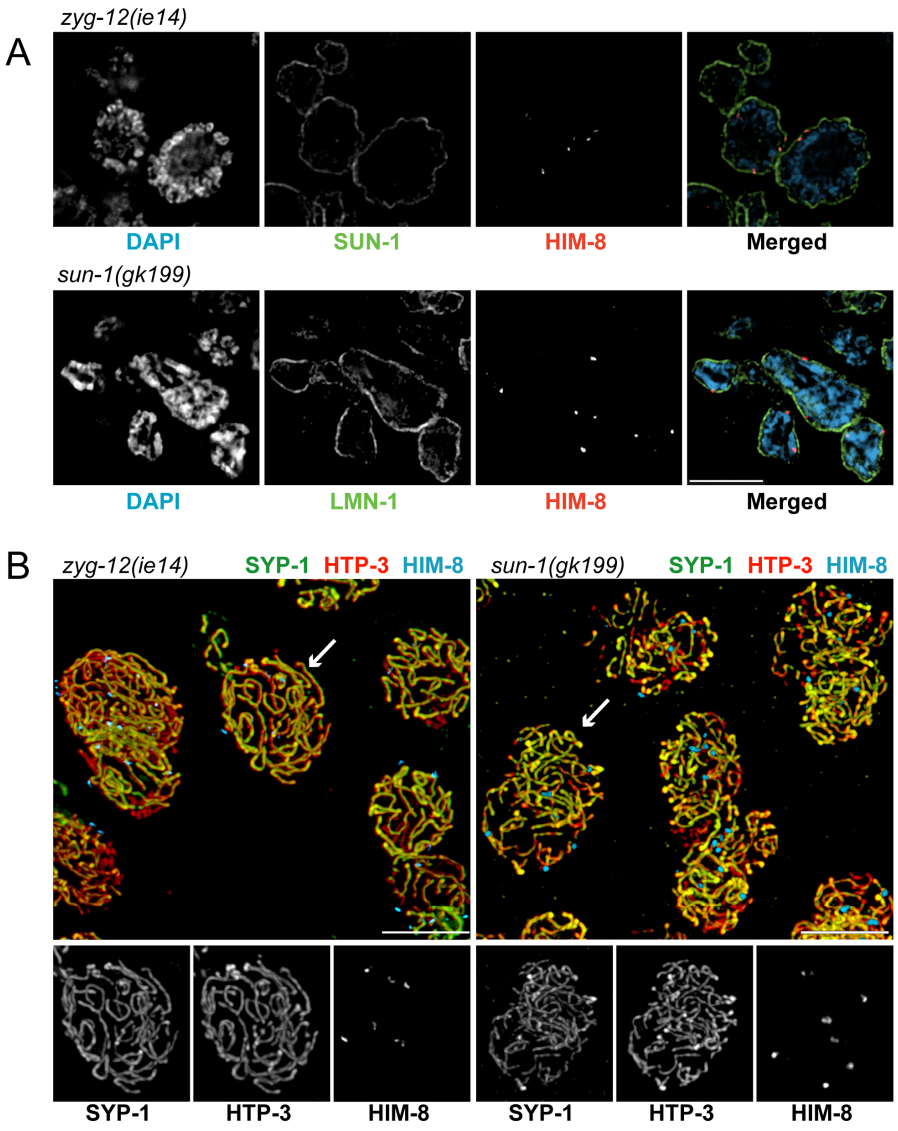

Figure S11. ZYG-12 and SUN-1 are dispensable for association of HIM-8 with the NE and for SC polymerization. (A) Cross-section views of nuclei from the mid-prophase region of homozygous *zyg-12(ie4)* or *sun-1(gk199)* hermaphrodites stained with anti-SUN-1 or anti-lamin (green), anti-HIM-8 (red), and DAPI (blue). These deletion mutants are sterile, but homozygous progeny of heterozygous parents survive to adulthood and have disorganized germlines containing many nuclei that show hallmarks of meiosis, including SC polymerization. Most meiotic nuclei show evidence of prior mitotic errors, such as severe polyploidy or fragmentation. In the absence of either SUN-1 or ZYG-12, HIM-8 foci are associated with the NE. These images are single optical sections, which more clearly reveal HIM-8 association with the NE than 3D projections. (B) Maximum-intensity projections showing nuclei from *sun-1(gk199)* or *zyg-12(ie14)* mutants, stained with antibodies against SYP-1 (green), HTP-3 (red) and HIM-8 (blue). Extensive SYP-1 loading was observed in the absence of either ZYG-12 (left) or SUN-1 (right). Separated fluorescence signals from individual polyploid nuclei, indicated by arrows in the top panels, are shown in the bottom panel. Scale bars, 5μm.

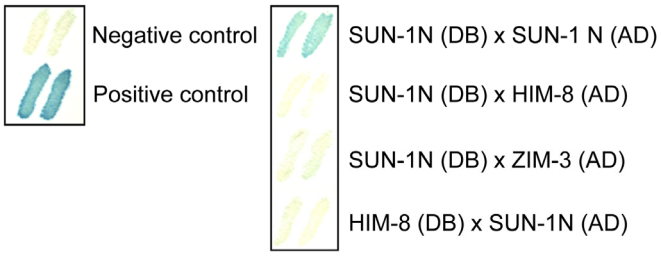

Figure S12. The amino-terminal region of SUN-1 can interact with itself, but not with HIM-8 or ZIM-3, in a Y2H assay. Yeast two-hybrid analysis was performed using ProQuest™ Two-Hybrid System (Invitrogen). Negative and positive controls are provided with the commercial vectors. DB: GAL-4 DNA binding domain, AD: GAL-4 activation domain. Amino acids 1-108 of SUN-1 (SUN-1N) and full-length HIM-8 and ZIM-3 were expressed in yeast from appropriate vectors and tested for pairwise interactions.

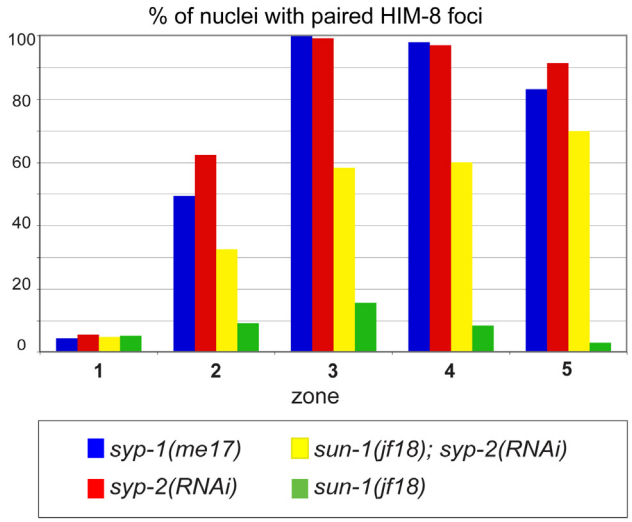

Figure S13. The *sun-1(jf18)* missense mutation reduces but does not abolish HIM-8 pairing. Pairing of the *X* chromosome PC was assessed following HIM-8 immunostaining. Gonads were divided into five zones of equal length, designated as zones 1, 2, 3, 4 and 5. At least three gonads were scored for each genotype. The total number of nuclei scored for zones 1, 2, 3, 4, and 5, respectively, was as follows: *syp-1(me17)* 130, 158, 162, 144, 107; *syp-2(RNAi)*: 87, 88, 124, 100, 81; *sun-1(jf18); syp-2(RNAi):* 138, 138, 147, 118, 70; *sun-1(jf18)*: 147, 171, 165, 139, 92. Similar analysis was performed by (Penkner et al., 2007), who reported somewhat lower levels of pairing at the *X* PC by FISH. We emphasize here that markedly higher levels of pairing are observed in *sun-1(jf18)* mutants in the absence of synapsis (compare *sun-1(jf18); syp-2(RNAi)* to *sun-1(jf18))*, indicating that the mutant protein is partially proficient for pairing but that precocious synapsis in this mutant results in very low levels of *X* chromosome pairing.

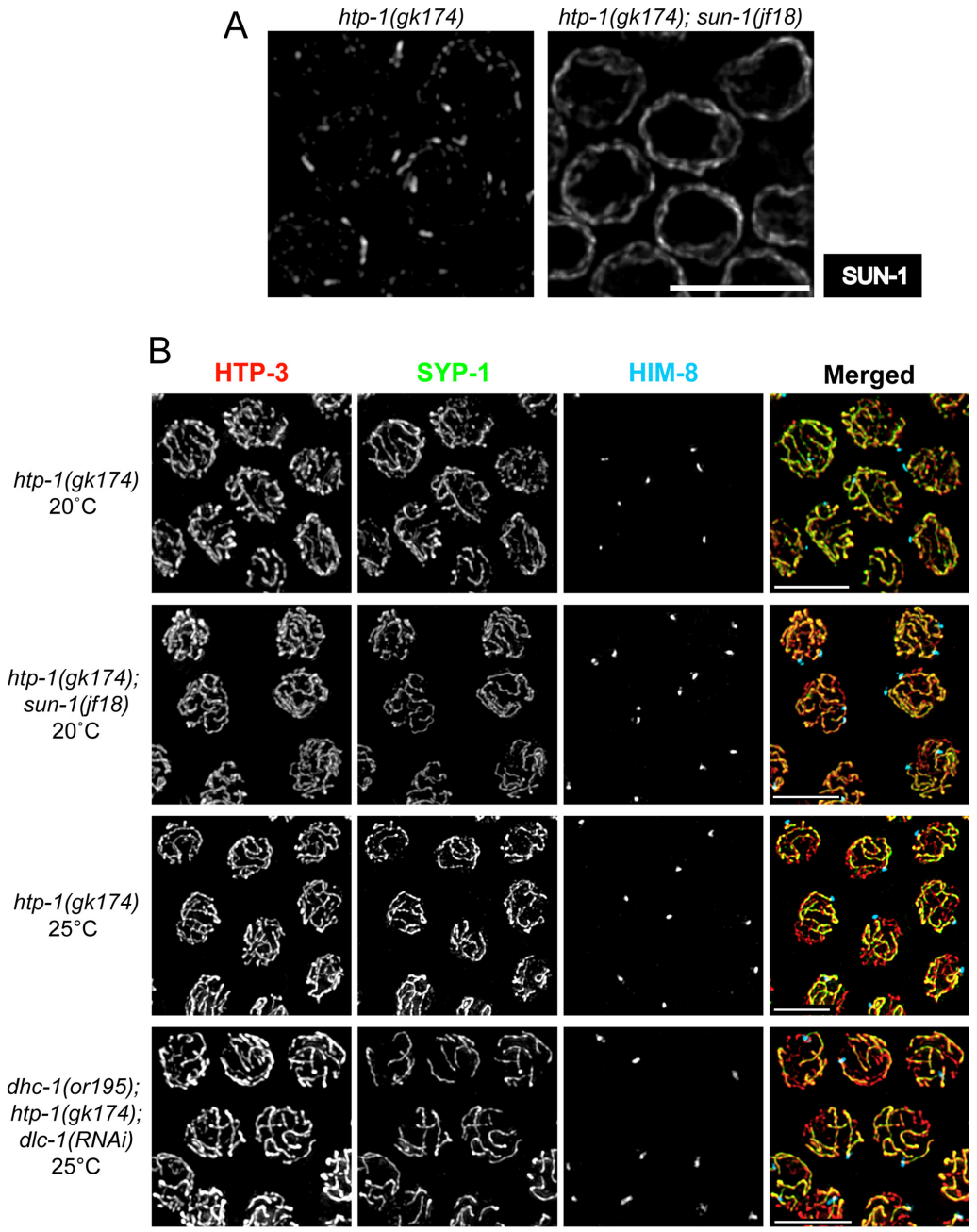

Figure S14. **HTP-1 contributes to a synapsis barrier independently of SUN-1**. (A) NE patches are observed in the absence of HTP-1. Early prophase nuclei from *htp-1(gk174)* and *htp-1(gk174); sun-1(jf18)* hermaphrodites are shown. Small SUN-1 patches were evident in *htp-1(gk174)* gonads, while distinct patches were not detected in *htp-1(gk174); sun-1(jf18)* nuclei. (B) Maximum-intensity projections showing HTP-3 (red), SYP-1 (green) and HIM-8 (blue) immunofluorescence. The *X* chromosomes undergo non-homologous synapsis in *htp-1(gk174); sun-1(jf18)* hermaphrodites, but synapsis is less extensive than in *sun-1(jf18)* (Penkner et al. 2007) or *sun-1(RNAi)* animals (Figure 6). Loss of HTP-1, like reduction of SUN-1, bypasses the requirement for dynein for SC polymerization. Scale bars, 5μm.

Genotype	Percent males (total no. of adults scored)
mnDp66/+; meDf2/+	9.2 (816)
sun-1(ok1282)/+	0.1 (1000)
sun-1(jf18)/+	0.78 (516)
zyg-12 (ie14)/+	0.1 (1098)
mnDp66/+; sun-1(ok1282)/+; meDf2/+	17.5 (778)
mnDp66/+; sun-1(jf18)/+; meDf2/+	13.1 (1036)
mnDp66/+; zyg-12(ie14)/+; meDf2/+	14.9 (1244)

Table S1. Production of male self-progeny

Table S1. Genetic interactions are detected between partial loss of PC function and mutations in *sun-1 or zyg-12*. Nondisjunction of the *X* chromosome was quantified as the frequency of males among adult self-progeny of hermaphrodites of the indicated genotypes. *meDf2* is a deficiency of the *X* chromosome PC (Villeneuve 1994). Nondisjunction in heterozygous *meDf2*/+ hermaphrodites is intermediate between wild-type and *meDf2* homozygotes (Villeneuve, 1994) and is increased when the dosage of *sun-1* or *zyg-12* is reduced by half (*sun-1*/+ or *zyg-12*/+).

Supplemental References

Couteau, F., and Zetka, M. (2005). HTP-1 coordinates synaptonemal complex assembly with homolog alignment during meiosis in C. elegans. Genes Dev 19, 2744-2756.

Gustafsson, M.G., Shao, L., Carlton, P.M., Wang, C.J., Golubovskaya, I.N., Cande, W.Z., Agard, D.A., and Sedat, J.W. (2008). Three-dimensional resolution doubling in wide-field fluorescence microscopy by structured illumination. Biophys J 94, 4957-4970.

Kremer, J.R., Mastronarde, D.N., and McIntosh, J.R. (1996). Computer visualization of three-dimensional image data using IMOD. J Struct Biol 116, 71-76.

Martinez-Perez, E., and Villeneuve, A.M. (2005). HTP-1-dependent constraints coordinate homolog pairing and synapsis and promote chiasma formation during *C. elegans* meiosis. Genes Dev 19, 2727-2743.

Mastronarde, D.N. (2005). Automated electron microscope tomography using robust prediction of specimen movements. J Struct Biol 152, 36-51.

Muller-Reichert, T., Hohenberg, H., O'Toole, E.T., and McDonald, K. (2003). Cryoimmobilization and three-dimensional visualization of *C. elegans* ultrastructure J Microsc 212, 71-80

Penkner, A., Tang, L., Novatchkova, M., Ladurner, M., Fridkin, A., Gruenbaum, Y., Schweizer, D., Loidl, J., and Jantsch, V. (2007). The nuclear envelope protein Matefin/SUN-1 is required for homologous pairing in C. elegans meiosis. Dev Cell 12, 873-885.

Phillips, C.M., and Dernburg, A.F. (2006). A family of zinc-finger proteins is required for chromosome-specific pairing and synapsis during meiosis in C. elegans. Dev Cell 11, 817-829.

Villeneuve, A.M. (1994). A cis-acting locus that promotes crossing over between X chromosomes in Caenorhabditis elegans. Genetics 136, 887-902.

Zhou, K., Rolls, M.M., Hall, D.H., Malone, C.J., and Hanna-Rose, W. (2009). A ZYG-12-dynein interaction at the nuclear envelope defines cytoskeletal architecture in the C. elegans gonad. J Cell Biol 186.